

Breaking dense integration limits: inverse-designed lithium niobate multimode photonic circuits

Received: 28 August 2025

Accepted: 12 December 2025

Published online: 21 December 2025

 Check for updates

Xu Han^{1,2,7}, Hu Jiang^{1,7}, Jie He¹, Zixu Zhu¹, Jiahui Su¹, Mei Xian Low², Yongheng Jiang³, Yu He⁴, Lantian Feng⁵, Thach. G. Nguyen², Andreas Boes⁶, Chengliang Pan¹, Guanghui Ren²✉, Yong Zhang⁴, Xifeng Ren⁵, Yonghui Tian³✉, Annan Mitchell² & Haojie Xia¹✉

Despite the growing interest in thin film lithium niobate (TFLN) as a material platform for photonic integrated circuits (PIC), its moderate refractive index, CMOS-incompatible fabrication processes and inherent material anisotropy still raise questions about achieving dense integration comparable to mature platforms like silicon photonics while preserving the superior properties of lithium niobate. Here we show a photonic inverse design method to enable miniaturization and dense integration of lithium niobate PIC components. As proofs-of-concept, we experimentally demonstrate ultra-compact mode-division (de)multiplexer ($19 \times 25 \mu\text{m}^2$), multimode waveguide crossing ($15 \times 15 \mu\text{m}^2$), and waveguide bends ($30 \mu\text{m}$ bending radius). The fabricated components are used to construct multimode photonic circuits for large-capacity data communications, demonstrating dense integration of over 10 waveguide elements within a 0.06 mm^2 chip area. By integrating electro-optic modulators on the same chip, high-speed data modulation is demonstrated with 120 Gbps data rate per channel alongside multimode signal transmission. This work is expected to advance 10-fold higher area density of passive components and optical path design in TFLN.

Modern photonic integrated circuits (PICs) are undergoing a paradigm shift toward dense integration, which is essential for scaling bandwidth, minimizing energy per bit, and supporting on-chip convergence of diverse optical functionalities¹. Achieving such advancements requires photonic platforms that offer not only high index contrast but also wide spectral transparency, strong nonlinear and electro-optic properties². Conventional silicon, silicon nitride and III–V platforms, while mature in CMOS-compatible processes, face inherent limitations

in nonlinear performance, electro-optic response, or material transparency. In this context, thin-film lithium niobate on insulator (TFLNOI) has emerged as a promising alternative that combines a wide optical transparency window, strong nonlinear optical performance and high-speed electro-optic modulation^{3,4}. Recent advances in TFLNOI-based electro-optic modulators have demonstrated unprecedented 100 GHz bandwidths and near-1V driving voltages at different wavelength ranges^{5,6}, enabling more than a tenfold footprint reduction

¹School of Instrument Science and Opto-electronics Engineering, Hefei University of Technology, Hefei, China. ²Integrated Photonics and Applications Centre (InPAC), School of Engineering, RMIT University, Melbourne, Australia. ³School of Physical Science and Technology, Lanzhou University, Lanzhou, Gansu, China. ⁴State Key Laboratory of Advanced Optical Communication Systems and Networks, Shanghai Jiao Tong University, Shanghai, China. ⁵Laboratory of Quantum Information, University of Science and Technology of China, Hefei, China. ⁶School of Electrical and Mechanical Engineering, The University of Adelaide, Adelaide, SA, Australia. ⁷These authors contributed equally: Xu Han, Hu Jiang. ✉e-mail: guanghui.ren@rmit.edu.au; tianyh@lzu.edu.cn; hjxia@hfut.edu.cn

compared to bulk lithium niobate counterparts. These breakthroughs, driven by applications such as terabit per second optical communications⁷, precision optical metrology⁸ and quantum photonic processors⁹, position TFLNOI as a versatile platform for multifunctional photonic systems. However, the relatively modest refractive index contrast in TFLNOI waveguides, especially those fabricated with partial etching, inherently limits the mode confinement¹⁰. Thus, device dimensions such as waveguide bending radius face limitations, which constrain the achievable chip integration density and challenge the scalability demands of large-scale PICs. To bridge the gap between TFLNOI's exceptional material properties and dense chip integration, advanced photonic design methods are emerging as powerful tools toward compact footprints while maintaining compatibility with fabrication processes.

Inverse design, which leverages intelligent optimization algorithms to explore a vast parameter space, can significantly improve multistage efficiency in device design, simulation and fabrication by enabling fast creation of complex optical structures, e.g., metasurface, with ultra-compact size, unprecedented precision and functionality^{11,12}. Significant breakthroughs have been achieved in silicon photonics during the last few years, with the device footprint scaled down to the micron level, paving the way to densely integrated on-chip optical systems^{13–16}. However, to obtain inverse-designed PIC components and complex optical systems in TFLNOI, the inherent barriers of material, method and fabrication process are particularly intractable. First, an X-cut TFLNOI platform experiences refractive index anisotropy in the y/z plane, and the traditional scalar-based inverse design methods are inappropriate to address the scenarios of anisotropic material. Although a Z-cut TFLNOI platform can avoid the material anisotropy in the plane of lithium niobate thin film¹⁷, the access to the strong electro-

optic coefficient of lithium niobate (r_{33}) requires laying out electrodes vertically, which is inconvenient for chip integration. Second, a tensor-based inverse design method can be extended to the X-cut TFLNOI platform by considering the impact of material anisotropy of lithium niobate¹⁸. However, a computational complexity increase is inevitable compared to that of traditional scalar-based inverse design methods, which brings higher requirements for computing resources and simulation time. Third, the generally used physical direct etching method for TFLNOI can induce a slanted waveguide sidewall, which limits the device feature size¹⁹, resulting in significant degradation and variability in device performance. Thus, the inverse designed lithium niobate photonics requires an overall optimization to overcome the material anisotropy and limited device feature size, while reserving the access to excellent material properties of lithium niobate.

In this work, we demonstrate inverse-designed high-density multimode photonic circuits for high-speed and large-capacity data communications in a silicon nitride-TFLNOI (X-cut) hybrid platform. As shown in Fig. 1a, integrated multimode photonics can enable large-scale signal parallelism and enhance the information capacity of PICs by introducing higher-order waveguide modes as data carriers²⁰, which has also attracted attention in optical computing²¹, sensing²² and spectroscopy²³. Unfortunately, the arbitrary routing of multimode signals is usually built in a large chip area, even in a high-indexed material platform, due to the radiation leakage and inter-mode coupling¹⁴. As shown in Fig. 1b–d, we design, fabricate and experimentally demonstrate an optical mode-division (de)multiplexer ($19 \times 25 \mu\text{m}^2$), a multimode waveguide crossing ($15 \times 15 \mu\text{m}^2$) and a multimode waveguide bend ($30 \mu\text{m}$ bending radius) for the first three quasi-transverse electrical modes (TE_0 , TE_1 and TE_2). The measured insertion losses are lower than 2.5 dB at the wavelength of 1550 nm,

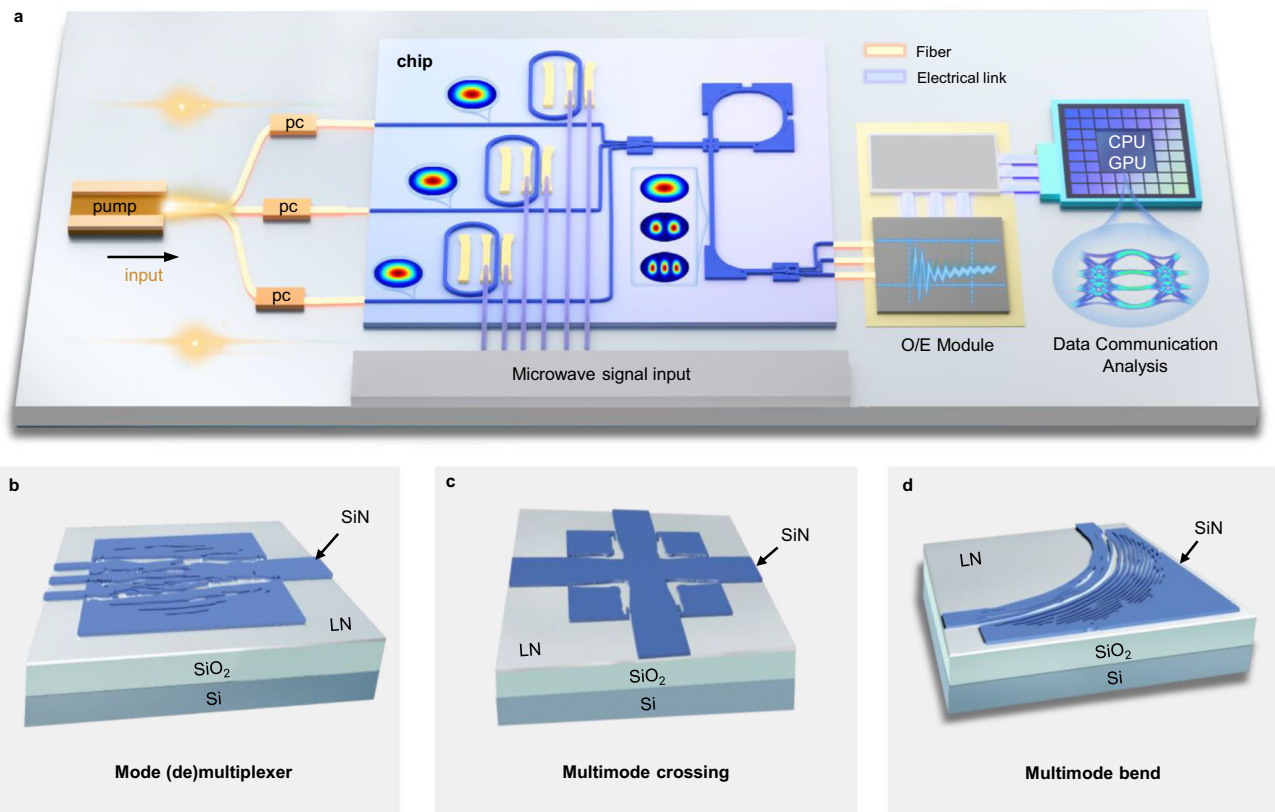


Fig. 1 | Inverse-designed lithium niobate multimode photonic circuits.

a Schematic diagram of an on-chip data modulation and multimode transmission system, where the chip consists of an array of micro-ring-based electro-optical modulators and the inverse-designed multimode photonic circuit (PC Polarization

Controller, O/E Optical/Electrical, CPU Central Processing Unit, GPU Graphics Processing Unit). **b–d** Schematic diagrams of the inverse-designed mode (de) multiplexer, multimode waveguide crossing and waveguide bend (SiN Silicon Nitride, LN Lithium Niobate, SiO₂ Silicon Dioxide, Si Silicon).

while the mode crosstalk stays below -15 dB at a wavelength range from 1530 nm to 1570 nm. These components are used to construct ultra-compact photonic circuits, enabling arbitrary routing of multimode signals through dense integration of more than 10 waveguide elements within a 0.06 mm^2 ($200 \times 300 \mu\text{m}^2$) chip area. To demonstrate the advancement in combination of high integration density with excellent material properties, a high-speed data modulation and transmission system is implemented through the monolithic integration of electro-optical modulators and multimode photonic circuits. The single-channel data modulation and transmission rate for on-off key signal reaches up to 120 Gbps.

Results

Waveguide platform

Silicon nitride is selected as an isotropic optical loading material. Thus, the optical structures in the loading layer can be optimized using a scalar-based inverse design method and fabricated by mature silicon nitride etching processes, enabling improved design efficiency and well-controlled device feature size. There are also other available loading materials, such as silicon, polymers and chalcogenide glasses. Among them, silicon is naturally an attractive loading material for dense integration since its high refractive index (-3.45 at 1550 nm) allows strong mode confinement in the loading rib, which can help to dramatically reduce the device footprint. However, the propagation loss of silicon-TFLNOI hybrid waveguide is relatively high²⁴, the lower mode confinement in lithium niobate thin film may lead to reduced electro-optical modulation and optical nonlinear efficiency²⁵, and the initial optical transparency window of silicon limits the waveguide's usefulness for nonlinear optical applications across a large wavelength range²⁶. By contrast, silicon nitride can be deposited by different methods with low optical loss, which offers a similar but slightly lower refractive index (-2.0 at 1550 nm) than lithium niobate ($n_e - 2.14$, $n_o - 2.22$ at 1550 nm), and similar optical transparency window spanning from visible to mid-infrared wavelengths compared with lithium niobate²⁷. The silicon nitride-TFLNOI (X-cut) hybrid platform is designed to avoid the direct etching of lithium niobate thin film, while providing a high mode confinement factor ($\sim 60\%$) in lithium niobate. The layers from top to bottom are air cladding, silicon nitride loading layer, lithium niobate slab, buried oxide layer and silicon substrate, respectively. A hybrid silicon nitride-TFLNOI ridge waveguide is formed by the deposited and etched silicon nitride loading rib and the unetched lithium niobate slab. Light is coupled to the hybrid ridge waveguide modes without evanescent coupling between different layers (see Supplementary Note 1 for details). The thicknesses of the silicon nitride and lithium niobate layers are both 300 nm, which avoids the mode lateral leakage at second-harmonic wavelengths²⁸. The thickness of the buried oxide layer is selected as $4.7 \mu\text{m}$ to ensure index match and a relatively low radio-frequency loss for electro-optic modulation.

Mode (de)multiplexer

Mode (de)multiplexers (MUXs) serve as critical PIC components to enable parallel propagation of multimodal signals in a single waveguide. Previous works in TFLNOI platform are generally based on directional coupler structures by forward design^{29–32}. In this case, the low-loss and low-crosstalk mode coupling relies on strict control of phase and mode field distribution, requiring a large device footprint. In contrast, in this contribution, we employ the inverse design method to implement a three-mode MUX with an ultra-compact effective size of only $19 \times 25 \mu\text{m}^2$.

Figure 2a, b shows an illustration and a scanning electron microscope (SEM) image of the device structure, which is designed and fabricated by patterning the silicon nitride layer. By considering the anisotropy of lithium niobate, the device is designed along the crystallographic Z direction to avoid the mode hybridization between TE_1 and TM_0 modes³³. The widths of the input single-mode waveguides

and output multimode waveguide are designed as $1 \mu\text{m}$ and $4.3 \mu\text{m}$, while the gaps between the adjacent input waveguides are $2 \mu\text{m}$. Compared with the directly etched TFLNOI waveguide, a near-vertical waveguide sidewall is available when etching silicon nitride, which means a smaller device feature size is allowed. The achievable smaller feature size enables creation of a refined waveguide structure, which is demonstrated to significantly improve the device performance, including insertion losses and mode crosstalk (see Supplementary Note 2 for details). To ensure fabrication reproducibility, we set the minimum feature size to 100 nm in this work.

We use two cascaded devices with the same structural parameters for signal multiplexing and demultiplexing in the experiment, as shown in Fig. 2c. Grating couplers are used as optical interfaces, which are designed with a period of 920 nm (940 nm for Y propagating) and a filling factor of 0.4³⁴. The simulated electric field profiles of a single device are monitored by using the three-dimensional finite-difference time-domain (3D-FDTD) method³⁵, at a wavelength of 1550 nm. As shown in Fig. 2d, the input TE_0 modes in the middle (l_0), upper (l_1) and lower (l_2) waveguides are coupled to TE_0 , TE_1 and TE_2 modes in the output waveguide, respectively. The corresponding transmission spectra at a wavelength range from 1530 nm to 1570 nm are depicted in Fig. 2e–g. The simulated insertion losses of the TE_0 , TE_1 and TE_2 modes are 0.52 dB, 0.63 dB, and 0.87 dB at the wavelength of 1550 nm, while the mode crosstalk stays below -20.1 dB across the whole wavelength range. To further characterize the device performance, the transmission spectra of different modes are measured by using the device shown in Fig. 2c. As shown in Fig. 2h–j, the measured insertion losses of TE_0 , TE_1 , and TE_2 mode channels are 1.05 dB, 1.42 dB, and 2.50 dB at the wavelength of 1550 nm, with the mode crosstalk lower than -15.9 dB across the whole wavelength range, which are in good agreement with the simulation results. The demonstrated MUX exhibits comparable performance with the conventional counterparts based on directional couplers (see Supplementary Note 3 for details), while representing a more than tenfold footprint reduction. Moreover, we have fabricated two other devices in which the widths of the etched waveguide patterns deviate from the optimal design by ± 20 nm. The measured results indicate that the fabricated device maintains low insertion loss, low mode crosstalk and wide bandwidth across fabrication variations, demonstrating good fabrication tolerance (see Supplementary Note 4 for details).

Multimode waveguide crossing

Waveguide crossing is another important PIC component for dealing with the cross connect in waveguide routing³⁶. The discontinuities at the intersection can induce mode coupling and interference, presenting inherent challenges for device design.

As shown in Fig. 3a, an ultra-compact three-mode waveguide crossing is designed with a device footprint of only $15 \times 15 \mu\text{m}^2$. The widths of the input and output multimode waveguides are $4.3 \mu\text{m}$, which are consistent with those of the MUX. As mentioned earlier, the minimum feature size is set to 100 nm, considering the trade-off between device performance and fabrication reproducibility. Figure 3b shows an SEM image of the fabricated device. To ensure the device performance, the electric field profiles of different modes are simulated at a wavelength of 1550 nm by using the 3D-FDTD method. As shown in Fig. 3c, the multimode signals pass through the waveguide crossing with negligible intermodal coupling and radiation loss. We characterize the waveguide crossing by using a pair of auxiliary MUXs based on directional couplers. The microscope image of fabricated devices is shown in Fig. 3d. The input TE_0 modes are coupled to different mode channels at the input ports, and then pass through the device. The multimode signals are demultiplexed at the output ports for transmission spectra measurements. The insertion losses of the fabricated waveguide crossing are measured through the cut-back method. As shown in Fig. 3e, the measured and fitted insertion losses of TE_0 , TE_1 , and TE_2

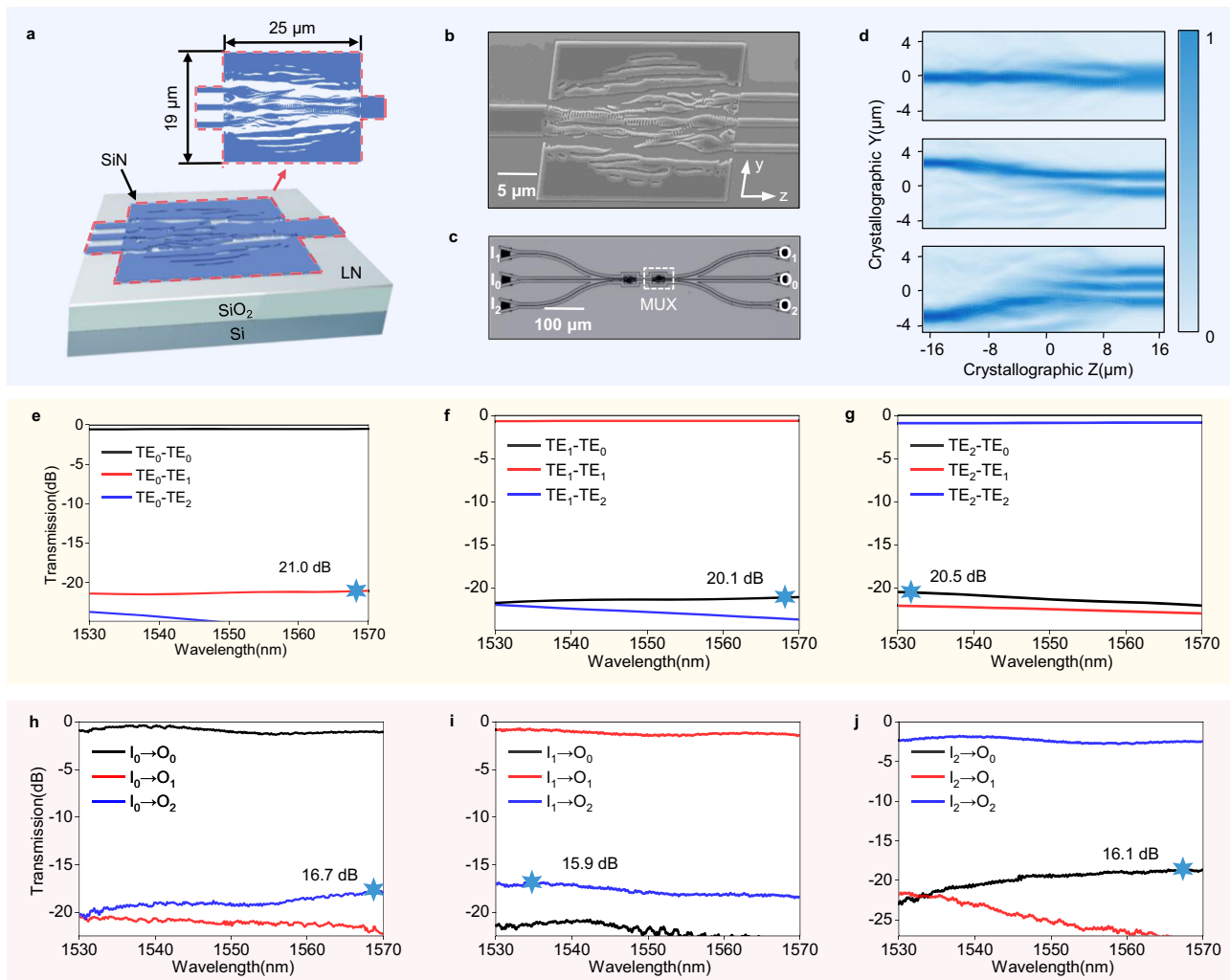


Fig. 2 | Design and experimental demonstration of MUX. **a** Illustration of the designed MUX with an effective size of $19 \times 25 \mu\text{m}^2$. **b** SEM image of the fabricated MUX with a minimum feature size of 100 nm. **c** Microscope image of the cascaded devices for signal multiplexing and demultiplexing in the experiment. **d** Simulated electric field profiles for the TE_0 mode input at different ports of the MUX. **e–g** Simulated transmission spectra of different mode channels at a wavelength

range from 1530 nm to 1570 nm. Black, red and blue lines represent the detected TE_0 , TE_1 and TE_2 modes, respectively, when light is injected into different channels. **h–j** Measured transmission spectra of different mode channels at a wavelength range from 1530 nm to 1570 nm. Black, red and blue lines represent the output signals at O_0 , O_1 and O_2 , respectively, when light is injected into I_0 , I_1 and I_2 ports.

modes at the wavelength of 1550 nm are 0.16 dB, 0.33 dB, and 0.55 dB, respectively. In addition to the ultra-low insertion losses, the fabricated waveguide crossing is also demonstrated to have low inter-modal crosstalk at a wide wavelength range from 1530 nm to 1570 nm. As shown in Fig. 3f–h, the simulated transmission spectra predict that the inter-modal crosstalk for TE_0 , TE_1 , and TE_2 mode channels stays below -19.4 dB, -46.2 dB and -18.9 dB. The corresponding measured results are shown in Fig. 3i–k, where the inter-modal crosstalk is lower than -17.7 dB, -15.0 dB and -16.1 dB for TE_0 , TE_1 , and TE_2 mode channels, respectively. We have noted that the crosstalk for the TE_1 mode channel is limited, due to the unexpected mode coupling in the auxiliary MUXs (see Supplementary Note 3 for details).

It should also be noted that the anisotropy of lithium niobate has been included in the device optimization. Thus, the designed and fabricated device has similar performance when light propagates along the crystallographic Z direction of lithium niobate (see Supplementary Note 5 for details).

Multimode waveguide bend

The waveguide bending radius is strongly limited in the TFLNOI platform due to the relatively low refractive index. The single-mode

waveguide bending radius in a micro-ring resonator typically reaches up to 80–100 μm , to reduce the mode mismatch and radiation losses^{37,38}. The multimode waveguide bends require a larger size, inevitably due to the weaker confinement for higher-order modes. Though shape optimization like Euler bends³¹, B-spline³⁹ or air grooves⁴⁰ can significantly reduce the multimode waveguide bending radius to 100–160 μm , there is still a gap between the size required for dense integration. Here, we demonstrate an ultra-compact multimode waveguide bend with an effective bending radius of only 30 μm , which is equivalent to that of the sharpest single-mode waveguide bend with a partial-etched waveguide cross-section in X-cut TFLNOI platforms^{41,42}, to the best of our knowledge.

The schematic diagram and SEM image of the multimode waveguide bend are shown in Fig. 4a, b. The widths of the input and output multimode waveguides are 4.3 μm . Figure 4c shows the electric field profiles of different modes, simulated by using the 3D-FDTD method at a wavelength of 1550 nm. After passing through the topology optimization area, the propagation directions of multimodal signals are turned by 90° with negligible inter-modal coupling. Similarly, we characterize the device by using the directional coupler-based auxiliary MUXs. The microscope image of fabricated devices is shown in

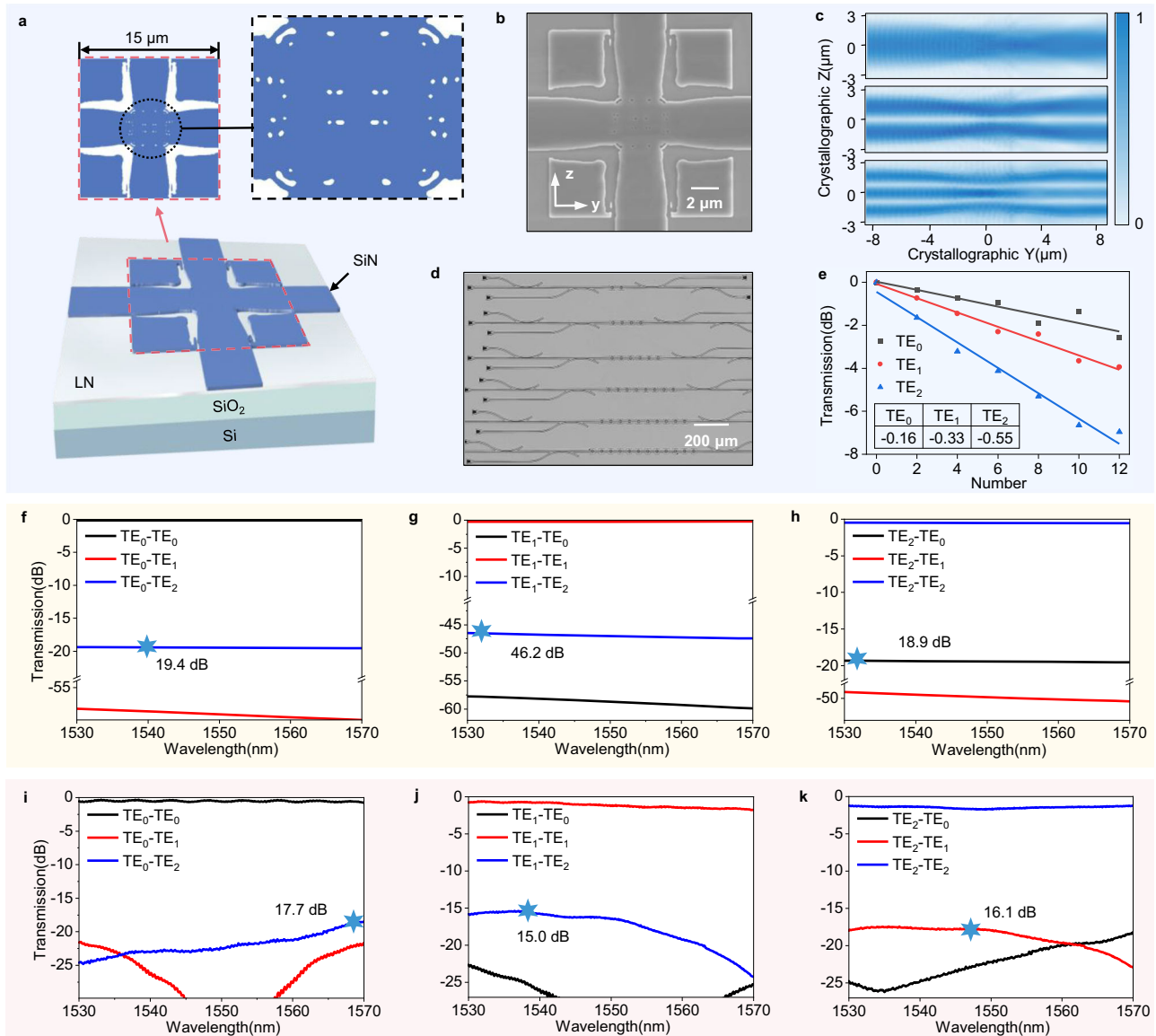


Fig. 3 | Design and experimental demonstration of multimode waveguide crossing. **a** Illustration of the designed waveguide crossing with an effective size of $15 \times 15 \mu\text{m}^2$. **b** SEM image of the fabricated device. **c** Simulated electric field profiles for different input modes: TE_0 , TE_1 and TE_2 . **d** Microscope image of the cascaded devices connected to auxiliary MUXs for insertion loss measurement. **e** Measured and fitted insertion losses of TE_0 , TE_1 , and TE_2 modes at the wavelength of 1550 nm.

Black, red and blue lines represent the fitted results of TE_0 , TE_1 , and TE_2 modes, respectively. **f–h** Simulated transmission spectra of different mode channels at a wavelength range from 1530 nm to 1570 nm. **i–k** Measured transmission spectra of different mode channels at a wavelength range from 1530 nm to 1570 nm. Black, red and blue lines represent the detected TE_0 , TE_1 and TE_2 modes, respectively, when light is injected into different channels.

Fig. 4d. The insertion losses of the fabricated waveguide bends are measured through the cut-back method. As shown in Fig. 4e, the measured and fitted insertion losses for TE_0 , TE_1 , and TE_2 modes at a wavelength of 1550 nm are 1.02 dB, 1.96 dB, and 2.17 dB, respectively.

The waveguide bend has low inter-modal crosstalk over a wide wavelength range. As shown in Fig. 4f–h, the simulation transmission spectra predict that the inter-modal crosstalk for TE_0 , TE_1 , and TE_2 mode channels can stay below -20.4 dB, -16.2 dB and -19.8 dB at a wavelength range from 1530 nm to 1570 nm. For the convenience of measurement, the propagation directions of the multimode signals are actually turned by 180° in the experiment (two 90° bends). The corresponding measured results are shown in Fig. 4i–k, where the inter-modal crosstalk for TE_0 , TE_1 , and TE_2 mode channels is lower than -16.2 dB, -15.1 dB and -15.9 dB, agreeing well with the simulated results. Moreover, we have performed an additional design for a single-mode 90° waveguide bend by using the same method. It is demonstrated that

the wide input and output waveguides offering strong mode confinement for the TE_0 mode can help to reduce the waveguide bending radius to about $14 \mu\text{m}$ (see Supplementary Note 6 for details).

Multimode photonic circuits

To further demonstrate the device performance in dense integration, we design and fabricate two types of multimode photonic circuits. The first PIC shown in Fig. 5a consists of two independent circuits with path crossing of the two circuits, while the second one shown in Fig. 5b is a single circuit with multipath crossings of the same circuit. The input fundamental modes are first coupled into different mode channels by the mode multiplexer. The multiplexed multimode signals are then routed in the chip plane by using the waveguide crossings and bends, which are finally demultiplexed by another mode demultiplexer. An only a chip area of $200 \times 300 \mu\text{m}^2$ is occupied to implement these operations.

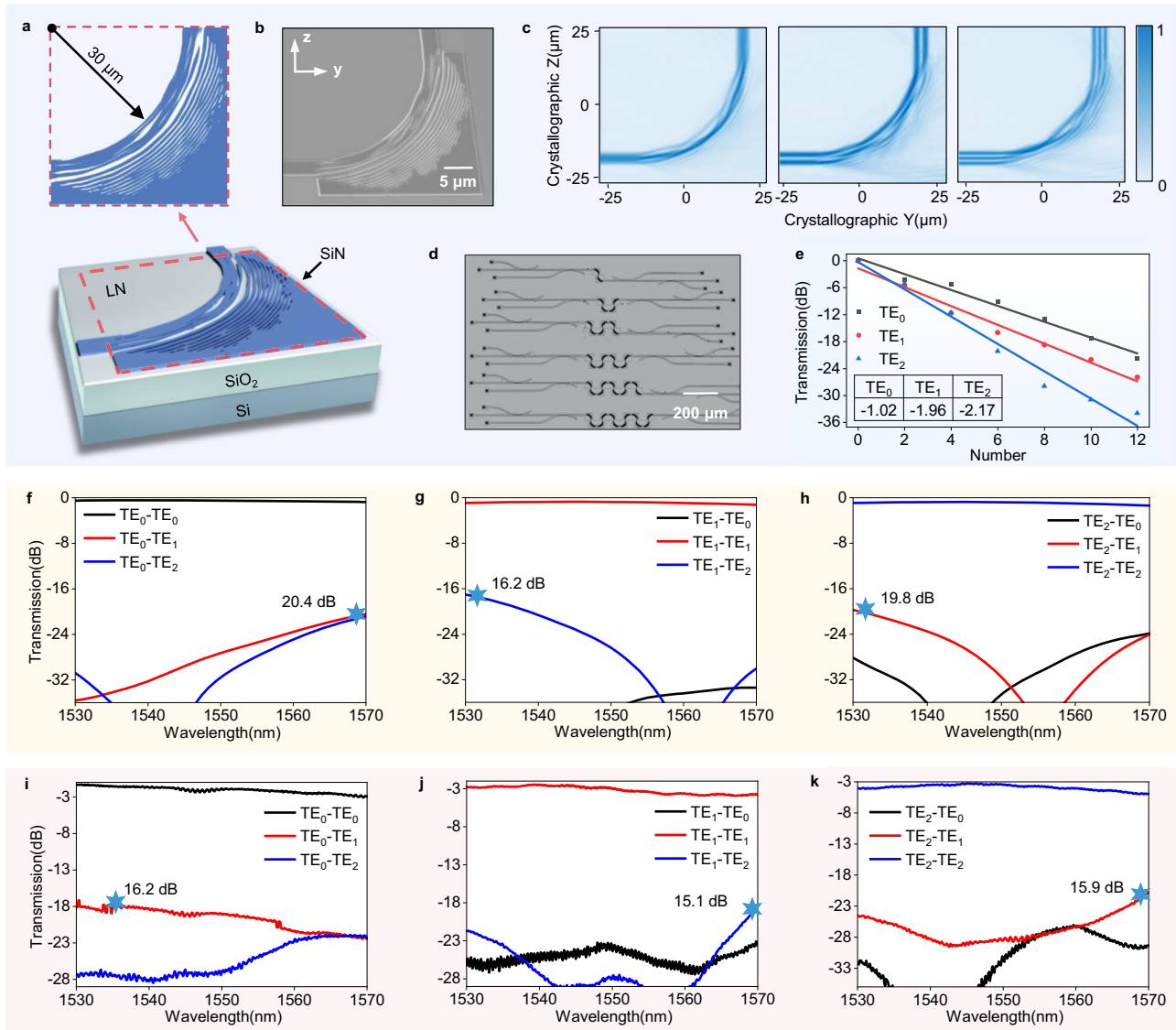


Fig. 4 | Design and experimental demonstration of multimode waveguide bend. **a** Illustration of the designed waveguide bend with an effective bending radius of 30 μm . **b** SEM image of the designed and fabricated device. **c** Simulated electric field profiles of different input modes. **d** Microscope image of the cascaded devices connected to auxiliary MUXs for insertion loss measurement. **e** Measured and fitted insertion losses of TE₀, TE₁, and TE₂ modes at the wavelength

of 1550 nm. Black, red and blue lines represent the fitted results of TE₀, TE₁, and TE₂ modes, respectively. **f–h** Simulated transmission spectra of different mode channels at a wavelength range from 1530 nm to 1570 nm. **i–k** Measured transmission spectra of different mode channels at a wavelength range from 1530 nm to 1570 nm. Black, red and blue lines represent the detected TE₀, TE₁ and TE₂ modes, respectively, when light is injected into different channels.

The measured transmission spectra of the first PIC are shown in Fig. 5c–e. The insertion losses for TE₀, TE₁ and TE₂ mode channels are 4.2 dB, 7.8 dB and 7.1 dB, while the inter-modal crosstalk stays below -20.3 dB at the wavelength of 1550 nm. Similarly, the measured transmission spectra of the second PIC are shown in Fig. 5f–h. It can be seen that the insertion losses for TE₀, TE₁ and TE₂ mode channels are 6.5 dB, 11.5 dB and 11.9 dB, while the inter-modal crosstalk still stays below -12.5 dB at the wavelength of 1550 nm. The measured insertion losses of PICs are very close to the sums of individual device insertion losses, with the deviations lower than 1 dB, 2.13 dB and 0.74 dB for TE₀, TE₁ and TE₂ modes (see Supplementary Note 7 for details). The deviations can be attributed to the following two aspects. First, the reported insertion losses of waveguide crossing and bends are measured and fitted by using the cut-back method. It can be seen from Figs. 3e, 4e that the measured insertion losses actually vary for different components in the experiment due to the fabrication variations. Second, the PICs and individual components are fabricated in different

regions on the same chip. Thus, the fabricated structural parameters for the same device can also be slightly different. Overall, despite a significant increase in the number of waveguide elements, the measured results still indicate good performance, presenting the good system scalability and dense integration capability of the inverse-designed devices.

To demonstrate the advancement in the combination of dense integration capability and excellent material properties, an on-chip data modulation and transmission system is implemented. We design and fabricate three electro-optical modulators based on the micro-ring resonator structure, corresponding to the employed three-mode channels. Light emitted by the lasers is modulated by high-speed radio-frequency signals, then routed in the chip plane by the multimode photonic circuits, and finally detected by photodetectors. A microscope image of the fabricated electro-optical modulator is shown in Fig. 6a. The designed waveguide width and the coupling gap are 1 μm and 750 nm, respectively. The radius of the ring waveguide is

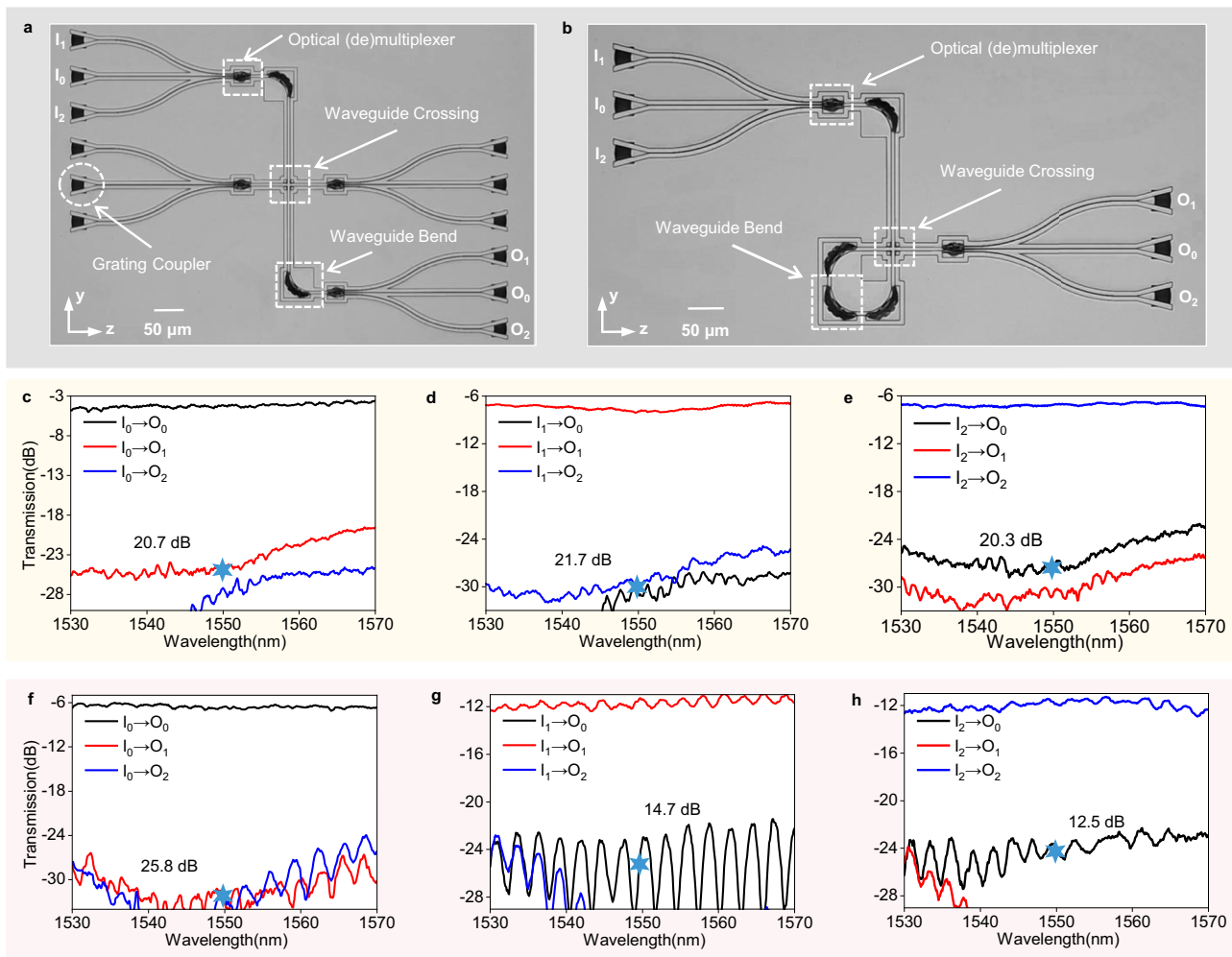


Fig. 5 | Experimental demonstration of multimode arbitrary routing system. a, b Microscope images of the fabricated multimode photonic circuits. **c–e** Measured transmission spectra of different mode channels for the first PIC, shown in (a). **f–h** Measured transmission spectra of different mode channels for the second PIC shown in (b). Black, red and blue lines represent the output signals at O_0 , O_1 and O_2 , respectively, when light is injected into I_0 , I_1 and I_2 ports.

300 μm , while the length of the straight track is 1.5 mm. The measured transmission spectrum of the micro-ring resonator is shown in Fig. 6b. The insertion loss at a non-resonant wavelength is lower than 0.54 dB, while the extinction ratio is larger than 12.4 dB. A ground-signal-ground (G-S-G) traveling-wave electrode is employed. The width of the signal electrode is designed as 23 μm , and the gap between signal and ground electrodes is 6 μm . Figure 6c shows the measured eye diagrams for different mode channels with the modulated and transmitted on-off key signal rates of 100 Gbps and 120 Gbps. The measured signal-to-noise ratios are larger than 5.4 dB. The clear and open eyes indicate good system performance.

Discussion

We compare the overall device performance, including effective size, insertion loss, mode crosstalk and data modulation rate, with previously reported works, as shown in Table 1. It can be seen that the measured insertion losses and inter-modal crosstalk are comparable with those of the forward-designed counterparts, while the device footprint is significantly reduced by an order of magnitude. Even compared with the previous single- or dual-mode devices, the demonstrated multimode devices exhibit relatively compact size, low insertion loss and low mode crosstalk. Moreover, the demonstrated PICs achieve similar high performance in electro-optical modulation when compared with the directly etched platforms, due to the high mode confinement in lithium niobate thin film.

We also compare the key performance metrics of recently reported inverse-designed devices on different material platforms, including silicon on insulator (SOI)^{15,43–46}, silicon nitride on insulator (SNOI)⁴⁷ and directly etched TFLNOI¹⁷. As shown in Table 2, the inverse-designed MUX serves as an illustrative example. Despite the moderate intrinsic refractive indices of both lithium niobate and silicon nitride, the demonstrated device achieves a footprint comparable to those in silicon photonics. Furthermore, it delivers similarly low loss and crosstalk as pure SNOI and TFLNOI devices, while uniquely combining the inverse design capabilities of silicon nitride with the strong electro-optic and nonlinear optical response of TFLN, offering a functionality set unavailable before. The device performance can be further improved through increasing the thickness of the deposited silicon nitride thin film, which can be attributed to enhanced interaction between light and the etched nanostructures due to the stronger mode confinement in the silicon nitride loading rib (see Supplementary Note 8 for details). However, the reduced mode confinement factor in lithium niobate thin film also means lower electro-optical modulation and optical nonlinear efficiency.

In summary, we have demonstrated ultra-compact multimode components and photonic circuits based on a silicon nitride-lithium niobate hybrid platform by using the photonic inverse design method. This hybrid platform shows a good combination of the excellent material properties of silicon nitride and lithium niobate. The optical structures in the isotropic silicon nitride loading layer are optimized by

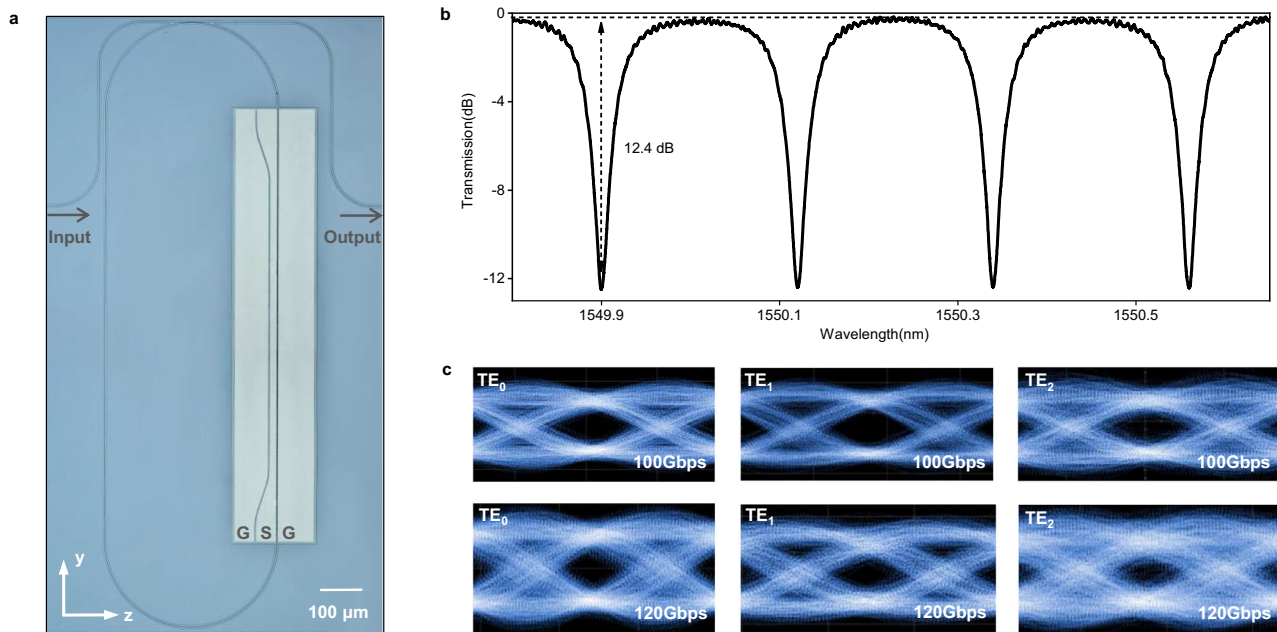


Fig. 6 | Experimental demonstration of on-chip data modulation and multi-mode signal transmission. a Microscope image of the fabricated micro-ring-based electro-optical modulator. **b** Measured transmission spectra of the micro-ring

resonator. **c** measured eye diagrams for different mode channels with the modulated and transmitted on-off key signal rates of 100 Gbps and 120 Gbps.

using a scalar-based inverse design method with improved design efficiency when compared with that using a tensor-based method for anisotropic materials. Moreover, the silicon nitride loading material owns mature fabrication processes, enabling improved device performance by means of small and well-controlled device feature size. The reduction in device footprint supports complex optical path design within an ultra-compact chip area, while more chip space is reserved for other important active functions such as data modulation, wavelength conversion, and spectral control. Our approach is scalable, which can be extended to a wide range of passive components, which are expected to be important building blocks for realizing densely integrated and large-scale PICs in the TFLNOI platform.

Methods

Inverse design method

Gradient optimization based on the adjoint method is used to implement topology optimization through iterative material distribution updates. The dielectric permittivity of the design area is initially projected onto a [0,1] space for parametric normalization (Eq. (1)). The material distribution is subsequently smoothed via a convolutional filtering (Eq. (2)) to eliminate subwavelength defects. Finally, an adaptive binarization projection function (Eq. (3)) is used to increase filter sharpness β and obtain a binary distribution of dielectric constants. We only need to optimize the distribution of isotropic silicon nitride loading material. Thus, the scalar-based inverse design method is applicable.

$$\rho_0 = \frac{\varepsilon_r(\rho) - \varepsilon_{min}}{\varepsilon_{max} - \varepsilon_{min}} \quad (1)$$

$$\rho_1 = w(x) \cdot \rho_0 \quad (2)$$

$$\rho_2 = \frac{\tanh(\beta \cdot \eta) + \tanh(\beta \cdot (\rho_1 - \eta))}{\tanh(\beta \cdot \eta) + \tanh(\beta \cdot (1 - \eta))} \quad (3)$$

where ρ_0 , ρ_1 and ρ_2 denote the normalized design parameters of the initial, filtered and binary design area, while $\varepsilon_r(\rho)$, ε_{min} and ε_{max}

represent the material dielectric constants of the design area, air cladding and silicon nitride load. In addition, $w(x)$ is the convolution kernel, β is the filter sharpness parameter, and η is the design threshold.

Device performance is quantified through a broadband figure of merit (FOM, Eq. 4).

$$FOM = \left(\frac{1}{\lambda_2 - \lambda_1} \int_{\lambda_1}^{\lambda_2} |T_0(\lambda)|^p d\lambda \right)^{1/p} - \left(\frac{1}{\lambda_2 - \lambda_1} \int_{\lambda_1}^{\lambda_2} |T(\lambda) - T_0(\lambda)|^p d\lambda \right)^{1/p} \quad (4)$$

where $T_0(\lambda)$, $T(\lambda)$ is the target and actual forward transmission at a wavelength of λ , while p is the generalized norm value which can control the optimization preference between transmission and bandwidth (see Supplementary Note 9 for details). In this instance, the effects of lithium niobate birefringence on device performance are included in the simulation.

Fabrication processes

We use an X-cut TFLNOI wafer from NanoLN, China. The silicon nitride thin film is deposited onto the chip by using a reactive sputtering process⁴⁸. The grating coupler and waveguide structures are patterned by using electron-beam lithography, and then formed by using single-step inductively coupled plasma etching. Finally, the electrodes (500-nm-thick Au) are fabricated by using laser direct writing, e-beam evaporation deposition and lift-off processes. The propagation losses of the fabricated waveguides are measured to be about 0.25 dB/cm by using the cut-back method. The coupling losses of the fabricated grating couplers are measured to be 6 dB/facet, at a peak coupling wavelength of 1560 nm.

Experimental setup

Light is emitted by a tunable laser, followed by a polarization controller used to maintain TE polarization before coupling light into the chip. For static measurements, signals coupled out of the chip are directed to an optical spectrum analyzer for spectral analysis.

For a high-speed data modulation and transmission experiment, the laser light is modulated by the on-chip electro-optical modulator

Table 1 | Performance comparison of some previously reported TFLN components

Refs	Device	Mode	Effective Size	Loss	Crosstalk	Modulation
29	MUX	TE ₀ ~ TE ₂	18 × 347 μm ²	<2.1 dB	<-17 dB	/
30	MUX	TE ₀ ~ TE ₂	22 × 500 μm ²	<4.69 dB	<-10.6 dB	/
31	MUX	TE ₀ ~ TE ₂	17 × 450 μm ²	≈0.2 dB	<-19 dB	/
32	MUX	TE ₀ ~ TE ₂	17 × 450 μm ²	<2.0 dB	<-12 dB	60 Gbps
This Work	MUX	TE ₀ ~ TE ₂	19 × 25 μm ²	<2.5 dB	<-15.9 dB	120 Gbps
17	Crossing	TE ₀	12 × 12 μm ²	0.48 dB	<-36 dB	/
36	Crossing	TE ₀	17.5 × 16 μm ²	0.07 dB	<-50 dB	/
This Work	Crossing	TE ₀ ~ TE ₂	15 × 15 μm ²	<0.55 dB	<-15 dB	120 Gbps
41	Bend	TE ₀	30 μm	<0.05 dB	/	/
31	Bend	TE ₀ ~ TE ₂	160 μm	0.026 dB	<-25 dB	/
40	Bend	TE ₀ ~ TE ₂	120 μm	<2.5 dB	<-12.2 dB	/
This Work	Bend	TE ₀ ~ TE ₂	30 μm	<2.17 dB	<-15.1 dB	120 Gbps
This Work	System	TE ₀ ~ TE ₂	200 × 300 μm ²	<11.9 dB	<-12.5 dB	120 Gbps

Table 2 | Performance comparison of some inverse-designed MUXs

Refs	Platform	Mode	Effective Size	Loss	Crosstalk
43	SOI	TE ₀ ~ TE ₄	6 × 10 μm ²	<3.94 dB	<-20.7 dB
44	SOI	TE ₀ ~ TE ₃	4.8 × 4.8 μm ²	<2.95 dB	<-13 dB
15	SOI	TE ₀ ~ TE ₃	6.5 × 6.5 μm ²	<1.5 dB	<-16.3 dB
45	SOI	TE ₀ ~ TE ₃	5.4 × 2.7 μm ²	<0.93 dB	<-13.5 dB
46	SOI	TE ₀ ~ TE ₂	6 × 4.8 μm ²	<4.3 dB	<-11.3 dB
47	SNOI	TE ₀ ~ TE ₄	16 × 7 μm ²	<2.3 dB	<-10.6 dB
17	TFLNOI (Z-cut)	TE ₀ , TE ₁	12 × 12 μm ²	<3.0 dB	<-15.8 dB
This work	SiN-TFLNOI (X-cut)	TE ₀ ~ TE ₂	19 × 25 μm ²	<2.5 dB	<-15.9 dB

using a $2^{10} - 1$ pseudo-random binary sequence generated by an arbitrary waveform generator. After coupling into and out of the chip, the signals are amplified by an erbium-doped fiber amplifier, followed by an optical tunable filter for reducing background noise. Finally, the signals are received by a digital communication analyzer for eye diagram measurements (see Supplementary Note 10 for details).

Data availability

All the data that support the findings of this study are included in the Article and its Supplementary Information. Source data are available via Figshare at <https://doi.org/10.6084/m9.figshare.30782306>.

References

- Su, Y. et al. Scalability of large-scale photonic integrated circuits. *ACS Photon* **10**, 2020–2030 (2023).
- Zhu, D. et al. Integrated photonics on thin-film lithium niobate. *Adv. Opt. Photon.* **13**, 242–352 (2021).
- Boes, A. et al. Lithium niobate photonics: unlocking the electromagnetic spectrum. *Science* **379**, 40 (2023).
- Hu, Y. et al. Integrated electro-optics on thin-film lithium niobate. *Nat. Rev. Phys.* **7**, 237–254 (2025).
- Wang, C. et al. Integrated lithium niobate electro-optic modulators operating at CMOS-compatible voltages. *Nature* **562**, 101–104 (2018).
- Valdez, F., Mere, V. & Mookherjee, S. 100 GHz bandwidth, 1 volt integrated electro-optic Mach–Zehnder modulator at near-IR wavelengths. *Optica* **10**, 578–584 (2023).
- Xu, M. et al. Dual-polarization thin-film lithium niobate in-phase quadrature modulators for terabit-per-second transmission. *Optica* **9**, 61–62 (2022).
- Qi, Y. et al. 1.79-GHz acquisition rate absolute distance measurement with lithium niobate electro-optic comb. *Nat. Commun.* **16**, 2889 (2025).
- Zhu, D. et al. Spectral control of nonclassical light pulses using an integrated thin-film lithium niobate modulator. *Light: Sci. Appl.* **11**, 1–9 (2022).
- Li, Z. et al. High-density lithium niobate photonic integrated circuits. *Nat. Commun.* **14**, 4856 (2023).
- Molesky, S. et al. Inverse design in nanophotonics. *Nature Photon* **12**, 659–670 (2018).
- Wei, H., He, X. & Cao, W. Spin-multiplexed metasurface inverse-design based on a bi-directional deep neural network for terahertz wavefront control. *Optica* **12**, 505–517 (2025).
- Piggott, A. et al. Inverse design and demonstration of a compact and broadband on-chip wavelength demultiplexer. *Nature Photon* **9**, 374–377 (2015).
- Liu, Y. et al. Arbitrarily routed mode-division multiplexed photonic circuits for dense integration. *Nat. Commun.* **10**, 3263 (2019).
- Yang, K. Y. et al. Multi-dimensional data transmission using inverse-designed silicon photonics and microcombs. *Nat. Commun.* **13**, 7862 (2022).
- Li, A. et al. An inversely designed integrated spectrometer with reconfigurable performance and ultra-low power consumption. *Opto-Electron. Adv.* **7**, 240099 (2024).
- Shang, C. et al. Inverse-designed lithium niobate nanophotonics. *ACS Photon* **10**, 1019–1026 (2023).
- Lyu, J. et al. Inverse design for material anisotropy and its application for a compact X-cut TFLN on-chip wavelength demultiplexer. *Opto-Electron. Sci.* **2**, 230038 (2023).
- Hu, H., Ricken, R. & Sohler, W. Lithium niobate photonic wires. *Opt. Express* **17**, 24261–24268 (2009).
- Luo, L. W. et al. WDM-compatible mode-division multiplexing on a silicon chip. *Nat. Commun.* **5**, 3069 (2014).
- Yin, R. et al. Integrated WDM-compatible optical mode division multiplexing neural network accelerator. *Optica* **10**, 1709–1718 (2023).
- Haider, F. et al. Mode-multiplex plasmonic sensor for multi-analyte detection. *Opt. Lett.* **45**, 3945–3948 (2020).
- Redding, B. et al. Evanescently coupled multimode spiral spectrometer. *Optica* **3**, 956–962 (2016).
- Wang, Z. et al. Silicon-lithium niobate hybrid intensity and coherent modulators using a periodic capacitively loaded traveling-wave electrode. *ACS Photon* **9**, 2668–2675 (2022).
- Chen, L. et al. Hybrid silicon and lithium niobate electro-optical ring modulator. *Optica* **1**, 112–118 (2014).

26. Green, M. A. Self-consistent optical parameters of intrinsic silicon at 300 K including temperature coefficients. *Sol. Energ. Mat. Sol. C.* **92**, 1305–1310 (2008).
27. Han, X. et al. Integrated photonics on the dielectrically loaded lithium niobate on insulator platform. *J. Opt. Soc. Am. B.* **40**, D26–D37 (2023).
28. Boes, A. et al. Improved second harmonic performance in periodically poled LNOI waveguides through engineering of lateral leakage. *Opt. Express* **27**, 23919–23928 (2019).
29. Han, X. et al. Integrated subwavelength gratings on a lithium niobate on insulator platform for mode and polarization manipulation. *Laser Photon. Rev.* **16**, 2200130 (2022).
30. Zhu, W. et al. Four-channel broadband mode (de)multiplexer based on thin-film lithium niobate platform. *ACS Photon* **11**, 2700–2706 (2024).
31. Zhao, W. et al. High-performance mode-multiplexing device with anisotropic lithium-niobate-on-insulator waveguides. *Laser Photon. Rev.* **17**, 2200774 (2022).
32. Zhao, W. et al. Mode-division-multiplexing transmitter with anisotropic lithium-niobate-on-insulator photonic waveguides. *Laser Photon. Rev.* **19**, 2400861 (2025).
33. Han, X. et al. Mode and polarization-division multiplexing based on silicon nitride-loaded lithium niobate on insulator platform. *Laser Photon. Rev.* **16**, 2100529 (2022).
34. Han, X. et al. Single-step etched grating couplers for silicon nitride-loaded lithium niobate on insulator platform. *APL Photon* **6**, 086108 (2021).
35. Scarmozzino, R. et al. Numerical techniques for modeling guided-wave photonic devices. *IEEE J. Sel. Top. Quantum Electron.* **6**, 150–162 (2000).
36. Chen, Y. et al. Design and resonator-assisted characterization of high-performance lithium niobate waveguide crossings. *Opt. Lett.* **48**, 2218–2221 (2023).
37. Guarino, A. et al. Electro-optically tunable microring resonators in lithium niobate. *Nat. Photon.* **1**, 407–410 (2007).
38. Zhang, M. et al. Monolithic ultra-high-Q lithium niobate microring resonator. *Optica* **4**, 1536–1537 (2017).
39. Xu, B. et al. High-performance B-spline multimode waveguide bends in lithium niobate on insulator. *Opt. Express* **33**, 13481–13493 (2025).
40. Ma, M. et al. Multimode waveguide bends in lithium niobate on insulator. *Laser Photon. Rev.* **17**, 2200862 (2023).
41. Liu, X. et al. Sharp bend and large FSR ring resonator based on the free-form curves on a thin-film lithium niobate platform. *Opt. Express* **32**, 9433–9441 (2024).
42. Wang, J. et al. Large free spectral range, high Q-factor microring resonator in thin-film lithium niobate photonics. *Opt. Lett.* **50**, 3094–3097 (2025).
43. Sun, A. et al. Edge-guided inverse design of digital metamaterial-based mode multiplexers for high-capacity multi-dimensional optical interconnect. *Nat. Commun.* **16**, 2372 (2025).
44. Zhou, H. et al. Dielectric metasurfaces enabled an ultradensely integrated multidimensional optical system. *Laser Photon. Rev.* **16**, 2100521 (2022).
45. Li, J. et al. Ultra-compact scalable mode demultiplexers for high-speed optical interconnects via GPU-accelerated inverse design. *Opt. Express* **33**, 44908–44924 (2025).
46. Sun, A. et al. On-chip multi-band mode-division multiplexed optical interconnect using ultra-broadband inverse-designed digital metamaterials. *Photon. Res.* **13**, 2831–2842 (2025).
47. Pita Ruiz, J. L., Dalvand, N. & Ménard, M. Integrated silicon nitride devices via inverse design. *Nat. Commun.* **16**, 9307 (2025).
48. Frigg, A. et al. Low-loss CMOS-compatible silicon nitride photonics utilizing reactive sputtered thin films. *Opt. Express* **27**, 37795–37805 (2019).

Acknowledgments

This work is supported by the National Natural Science Foundation of China (62405082, T2325022), Natural Science Foundation of Anhui Province (2408085QF217) and Fundamental Research Funds for the Central Universities (JZ2023HGQA0479, JZ2024HGTA0185). The authors acknowledge the facilities and the scientific and technical assistance of the Micro Nano Research Facility (MNRF) and the Australian Microscopy & Microanalysis Research Facility at RMIT University. This work was performed in part at the Melbourne Center for Nanofabrication (MCN) in the Victorian Node of the Australian National Fabrication Facility (ANFF). This work was performed in part at the OptoFab node of the Australian National Fabrication Facility, utilizing NCRIS and VIC state government funding. A.B. is supported by an ARC DECRA fellowship (DE230100964).

Author contributions

X.H. conceived the project. H.J. performed the numerical simulations. M.X.L. and G.R. fabricated the chips. X.H. and H.J. established the static measurement setup and performed the transmission spectra analysis. Y.J. and Y.T. established the dynamic measurement setup and performed the high-speed data modulation and transmission experiment. X.H., H.J., J.H., Z.Z., J.S., Y.J., and G.R. discussed and analyzed the measured results. Y.H., L.F., T.G.N., A.B., C.P., Y.Z., X.R., Y.T., A.M., and H.X. participated in preparing the manuscript and contributed to the discussions. X.H. and H.J. wrote the paper draft and revised it based on the comments from all authors. The project was performed under the supervision of G.R., Y.T., and H.X.

Competing interests

The authors declare no competing interests.

Additional information

Supplementary information The online version contains supplementary material available at <https://doi.org/10.1038/s41467-025-67927-7>.

Correspondence and requests for materials should be addressed to Guanghui Ren, Yonghui Tian or Haojie Xia.

Peer review information *Nature Communications* thanks Dawn Tan and the other anonymous reviewer(s) for their contribution to the peer review of this work. A peer review file is available.

Reprints and permissions information is available at <http://www.nature.com/reprints>

Publisher's note Springer Nature remains neutral with regard to jurisdictional claims in published maps and institutional affiliations.

Open Access This article is licensed under a Creative Commons Attribution-NonCommercial-NoDerivatives 4.0 International License, which permits any non-commercial use, sharing, distribution and reproduction in any medium or format, as long as you give appropriate credit to the original author(s) and the source, provide a link to the Creative Commons licence, and indicate if you modified the licensed material. You do not have permission under this licence to share adapted material derived from this article or parts of it. The images or other third party material in this article are included in the article's Creative Commons licence, unless indicated otherwise in a credit line to the material. If material is not included in the article's Creative Commons licence and your intended use is not permitted by statutory regulation or exceeds the permitted use, you will need to obtain permission directly from the copyright holder. To view a copy of this licence, visit <http://creativecommons.org/licenses/by-nc-nd/4.0/>.

© The Author(s) 2025